scientific reports

Check for updates

OPEN

Application of virtual monochromatic images in bone mineral density measurements: a phantom study

Yi Shu[1,3], Yiteng Zhang[1,3], Ziqi Chen[1], Pei Yang[1], Zheng Ye[1], Tianjiao Lan[2], Zhenlin Li[1,3✉] & Jing Tang[1,3✉]

Quantitative CT (QCT) measures bone mineral density (BMD), but beam hardening effect can cause errors and instability in BMD measurements. The purpose of this phantom study is to explore whether the application of virtual monochromatic images (VMIs) in QCT can reduce the measurement error of BMD, and determine the VMI levels that can minimize the error with different radiation doses and regions of interest (ROI) sizes. Utilizing a spine phantom with established hydroxyapatite concentrations, we performed scans with a CT scanner employing rapid tube voltage switching in both single-energy and dual-energy modes. A range of radiation doses (12 mGy, 15 mGy, and 24.4 mGy) was administered, and dual-energy data were reconstructed into VMIs spanning 60–76 keV in 1-keV increments. BMD was measured using regions of interest (ROIs) of varying sizes, and measurements were systematically recorded and compared across all protocols. Our findings indicate that both radiation doses and ROI sizes significantly impacted BMD measurements ($P < 0.001$). Importantly, BMD values exhibited a consistent decline with increasing VMI levels (r_s: -0.990 to -0.998, $P < 0.001$), while measurements derived from 120-kVp images tended to be slightly elevated compared to actual hydroxyapatite concentrations ($P < 0.001$). Among the evaluated VMIs, the 74-keV level provided the most reliable BMD measurements while ensuring acceptable accuracy. In conclusion, the integration of VMIs in QCT significantly minimizes measurement errors in BMD assessments relative to traditional 120-kVp imaging methods, highlighting their potential to enhance diagnostic accuracy in clinical settings.

Keywords Virtual monochromatic image, Bone mineral density, Quantitative computed tomography, Phantom

Abbreviations

AI	Artificial intelligence
BMD	Bone mineral density
DECT	Dual-energy computed tomography
ESP	European spine phantom
HA	Hydroxyapatite
kVp	Peak tube voltage
L1	The first lumbar vertebra
L2	The second lumbar vertebra
L3	The third lumbar vertebra
MSE	Mean squared error
OLS	Ordinary least squares
PCD-CT	Photon-counting detector computed tomography
QCT	Quantitative computed tomography
ROI	Region of interest

[1]Department of Radiology, West China Hospital of Sichuan University, No. 37 Guoxue Alley, Chengdu 610041, Sichuan, China. [2]HEOA Group, West China School of Public Health and West China Fourth Hospital of Sichuan University, No.18 Renmin South Road, Chengdu 610041, Sichuan, China. [3]Yi Shu and Yiteng Zhang were co-first authors and contributed equally to this work; Zhenlin Li and Jing Tang were co-corresponding authors and contributed equally to this work. ✉email: HX_lizhenlin@126.com; tangjing@wchscu.cn

VMI	Virtual monochromatic image

Quantitative computed tomography (QCT) is widely used to measure spinal bone mineral density (BMD) for diagnosing osteoporosis. QCT calculates BMD using 3D data, avoiding interference from overlapping blood vessels and organs[1]. Previous studies have shown that BMD measured by QCT is more accurate than dual-energy X-ray absorptiometry, mainly due to better correlation with clinical indicators and more sensitive to changes in bone mineral metabolism[1–4].

However, several factors can cause errors in BMD measurements based on QCT, such as imaging equipment, acquisition parameters, patient variables, calibration methods, etc.[5]. Currently, 120-kVp polychromatic X-rays are predominantly used in QCT examinations, with beam hardening being a major contributing factor to measurement errors. Based on the attenuation characteristics of high and low energy X-rays, dual-energy CT (DECT) can synthesize virtual images similar to those obtained by monochrome X-rays at different energy levels, which is called virtual monochromatic images (VMI) or virtual monoenergetic images[6]. The VMIs at 65–75 keV has been shown to have similar attenuation compared to 120-kVp polychromatic images, with less image noise and improved contrast-to-noise ratio[7]. Several studies have demonstrated the superiority of DECT in bone mineral density measurements, as well as the accuracy of BMD values based on spectral data[8,9]. While VMI has shown potential for artifact reduction in CT-based BMD assessment, its systematic integration with established phantom-calibrated QCT protocols remains underexplored, particularly regarding the optimization of energy levels for minimizing measurement variability across diverse clinical scenarios.

In this paper, we compared the BMD measurements of conventional 120-kVp polychromatic images with VMIs at 60–76 keV by using a vertebral phantom with known hydroxyapatite (HA) concentration, and explored the optimal VMI level for BMD measurement based on QCT. Meanwhile, we simulated different imaging protocol and subject body types by varying the radiation dose and the size of the region of interest (ROI) to verify whether these factors have an impact on the optimal VMI level.

Materials and methods

As a phantom study, this work did not involve any animals or subjects, so it did not require approval from the local ethics committee.

Phantom

An anthropomorphic European Spine Phantom (ESP, QRM-50100, QRM GmbH, Moehrendorf, Germany) was used[10]. The ESP comprises HA-containing epoxy resin, which can be modeled as HA and water for X-ray attenuation analysis[11]. To cover the full physiological range of BMD for spongy and cortical bone across all age groups, the phantom contains three inserts representing trabecular bone compartments: first lumbar vertebra (L1), with a HA concentration of 50 mg/cm³; second lumbar vertebra (L2), with a HA concentration of 100 mg/cm³; and third lumbar vertebra (L3), with a HA concentration of 200 mg/cm³. CT images of ESP are shown in Fig. 1, with L1, L2, and L3 successively from top to bottom, showing the difference in HA concentration among the three vertebral inserts.

QCT calibration and image acquisition

Imaging procedures were performed using a 256-detector-row CT scanner (Revolution CT, GE Healthcare, Waukesha, WI, USA) equipped with rapid tube voltage switching capability. Both conventional and dual-energy acquisition modes were employed for ESP imaging. The conventional acquisition protocol utilized a fixed 120-kVp tube voltage. Dual-energy acquisitions employed instantaneous tube voltage switching between 80 and 140 kVp, and set precise VMI reconstruction parameters for each scan (the reconstruction energy level range is 60–76 keV, and only the image of one energy level is reconstructed for each scan). CT scans were performed at three distinct volume CT doses index (CTDIvol) levels: 12 mGy, 15 mGy, and 24.4 mGy. These values were selected to represent the first, second, and third quartiles of radiation dose distributions specified for lumbar spine diagnostic protocols under Chinese National Occupational Health Standards[12]. Comprehensive scanning parameters are detailed in Table 1.

Prior to each experimental scan, system calibration was performed according to manufacturer specifications. The standard QCT calibration phantom (model 4, Mindways, Austin, TX, USA) underwent sequential conventional (120 kVp) and dual-energy (80/140 kVp) protocol scans. Acquired DICOM data were subsequently processed through the quality control module of the QCT software (CliniQCT, version 5.0, Mindways, Austin, TX, USA). Successful calibration was confirmed by system-generated "PASS" verification. Before each scan begins, Model4 needs to be used to calibrate the subsequent scan parameters. After the calibration is passed, an experimental scan of ESP is conducted. In the dual-energy scanning mode, each time the VMI reconstruction parameters are changed, a new calibration scan is required.

All the scanning protocols were scanned five times repeatedly in the experimental procedures. The average of the measured values of the five scanning data was included in the statistics to ensure the reliability of the data.

BMD measurement

All the scanning data were transmitted successively to the QCT software for BMD measurement. For each scan protocol, two sizes of ROI were used to measure BMD: the default size (249.8 mm²) and the maximum size (470 mm²). All ROIs were centrally placed in the bone trabecular compartment, ensuring that the position did not shift. The software automatically calculates BMD values based on 3D data according to the outlined ROI, and all BMD values are recorded.
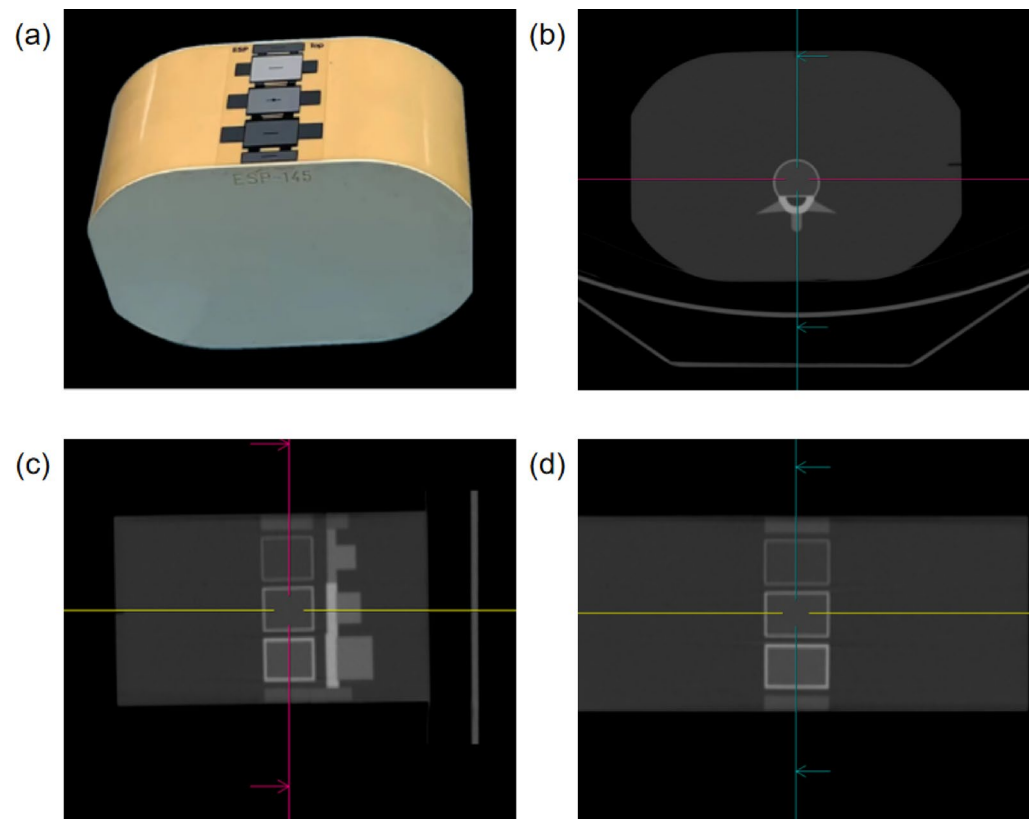
Fig. 1. European spine phantom (ESP). Photograph (**a**); Axial (**b**), Sagittal (**c**), and Coronal (**d**) CT tomographic images.

Parameter	Conventional mode			Dual-energy mode		
	Group A1	Group A2	Group A3	Group B1	Group B2	Group B3
Scanner mode	Helical			GSI Helical		
CTDIvol (mGy)	12	15	24.4	12	15	24.4
Peak tube voltage (kVp)	120			80–140		
Tube current (mA)	220	275	610	300	370	445
Rotation time (s)	0.8	0.8	0.6	0.8	0.8	1.0
Pitch	0.992	0.992	0.992	0.992	0.992	0.984
ASIR-V (%)	50			50		
Display FOV (cm)	50			50		
Slice thickness (mm)	1.25			1.25		
Slice interval (mm)	1.25			1.25		
VMI reconstruction	No			60–76 keV		

Table 1. Protocols for quantitative computed tomography in this study. *CTDIvol* volume computed tomography dose index, *GSI* gemstone spectral imaging, *FOV* field of view, *ASIR-V* iterative reconstruction.

Statistical analysis

All statistical analyses were performed using IBM SPSS Statistics (V22.0, IBM Corporation, Armonk, NY, USA), GraphPad Prism (V9.3.1, GraphPad Software, Boston, USA) and R software (V4.4.0, R Foundation for Statistical Computing, Vienna, Austria).

All quantitative data were tested for normality using the Shapiro–Wilk test, with quantitative data conforming to normal distribution expressed as mean ± standard deviation, quantitative data not conforming to normal distribution expressed as median (interquartile range). The Wilcoxon signed rank test was used to compare BMD measurements between different ROI sizes (default and maximum) at the same radiation dose. The one-sample T-test was used to compare BMD measurements with true HA concentrations. Spearman's correlation coefficient (r_s) described the relationship between VMI energy levels and BMD measurements. Univariate linear
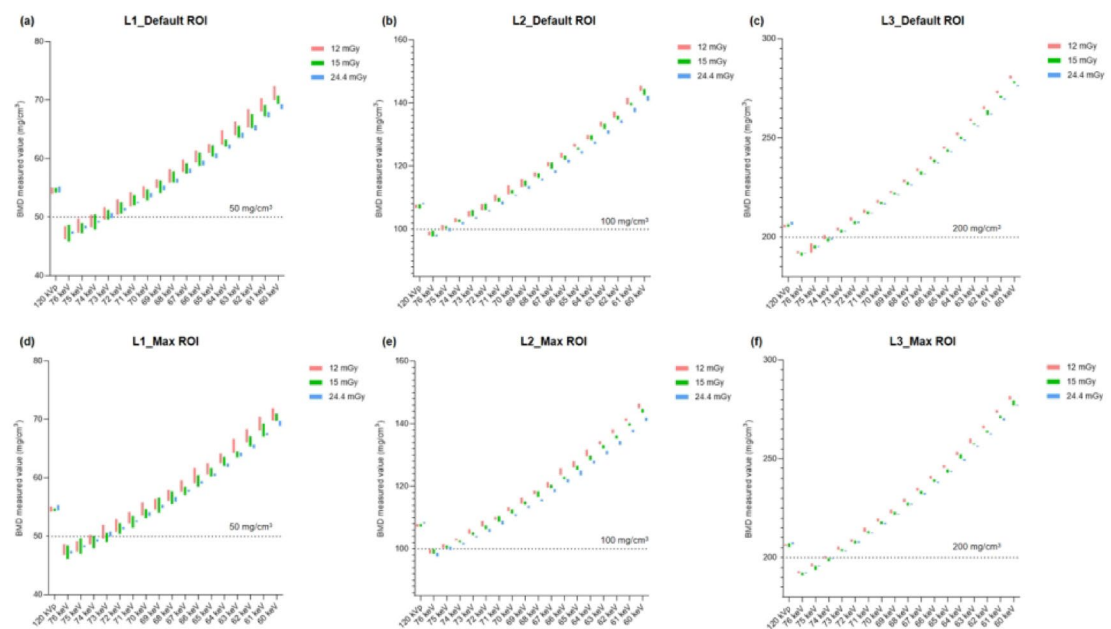
Fig. 2. BMD measurements based on 120-kVp images and VMIs at 60–76 keV with different ROI sizes and radiation doses. The dashed lines represent the true HA concentration of the corresponding vertebral insert. *BMD* bone mineral density, *HA* hydroxyapatite, *kVp* peak tube voltage, *ROI* region of interest, *VMI* virtual monochromatic image.

CTDIvol	BMD measurement (mg/cm³)		Z	P
	Max ROI	Default ROI		
12 mGy	117.0 (142.7)	116.2 (142.5)	− 9.076	< 0.001
15 mGy	115.9 (144.0)	115.8 (143.7)	− 5.979	< 0.001
24.4 mGy	114.5 (144.9)	114.6 (144.6)	− 8.475	< 0.001
F	14.73	9.49		
P	< 0.001	< 0.001		

Table 2. Comparison of the BMD measurements based on all CT images with different ROI sizes and radiation doses. The data is presented as the median, with interquartile spacing in parentheses. *BMD* bone mineral density, *ROI* region of interest, *CTDIvol* volume computed tomography does index.

models were used to compare BMD differences between radiation doses (12 mGy, 15 mGy, and 24.4 mGy) at the same ROI size.

Next, ordinary least squares (OLS) regression was used to explore the optimal VMI level under the influence of ROI size and radiation dose on BMD measurements. Considering the stability of BMD values measured at the same voltage, we further developed an estimate, *mean squared error (MSE)*: $MSE = B^2 + V$. In this formula, *V* represents variance, overpowering the previous estimate by combining both bias and variance. We compared the *MSE* of VMIs at different keV level and determined the optimal VMI level, that is, the VMI level with the lowest *MSE*.

In this study, the test level $\alpha = 0.05$, that is, $P < 0.05$ was considered to have statistical difference.

Results

In this study, we measured BMD of three lumbar inserts based on all CT images (both 120-kVp images and VMIs at 60–76 keV) with different ROI sizes and radiation doses. The measurement results are shown in Fig. 2 and Table 2. The statistical results in Table 2 showed that differences in ROI and radiation dose lead to differences in BMD measurements ($P < 0.001$), and BMD measurements may be affected by ROI and radiation dose. Figure 2 shows BMD measurements for all imaging protocols (scan mode, ROI size, radiation dose). For VMIs at 60–76 keV, BMD measurements gradually decrease as energy levels increase (r_s: − 0.990 to − 0.998, $P < 0.001$, Table 3).

The mean BMD values measured based on 120-kVp images and VMIs at 72–76 keV are listed in Table 4, and we conducted a one-sample T-test between them and the real HA concentration (Table S1). One-sample T-test

| Vertebral inserts	ROI size	Radiation dose		
		12 mGy	15 mGy	24.4 mGy
L1	Default	− 0.990 [− 0.994, − 0.985] (P < 0.001)	− 0.992 [− 0.995, − 0.988] (P < 0.001)	− 0.998 [− 0.999, − 0.997] (P < 0.001)
	Max	− 0.994 [− 0.996, − 0.990] (P < 0.001)	− 0.994 [− 0.996, − 0.991] (P < 0.001)	− 0.998 [− 0.999, − 0.997] (P < 0.001)
L2	Default	− 0.998 [− 0.999, − 0.997] (P < 0.001)	− 0.998 [− 0.999, − 0.997] (P < 0.001)	− 0.998 [− 0.999, − 0.997] (P < 0.001)
	Max	− 0.998 [− 0.999, − 0.997] (P < 0.001)	− 0.998 [− 0.999, − 0.997] (P < 0.001)	− 0.998 [− 0.999, − 0.997] (P < 0.001)
L3	Default	− 0.998 [− 0.999, − 0.997] (P < 0.001)	− 0.998 [− 0.999, − 0.997] (P < 0.001)	− 0.998 [− 0.999, − 0.997] (P < 0.001)
	Max	− 0.998 [− 0.999, − 0.997] (P < 0.001)	− 0.998 [− 0.999, − 0.997] (P < 0.001)	− 0.998 [− 0.999, − 0.997] (P < 0.001)

Table 3. Spearman's correlation coefficient between VMI levels and BMD measurements. The data is presented as Spearman's correlation coefficient (r_s), with 95% confidence intervals in square brackets and P values in parentheses. *BMD* bone mineral density, *ROI* region of interest, *VMI* virtual monochromatic image.

Radiation dose (mGy)	Modes	Default ROI			Max ROI		
		L1 (mg/cm³)	L2 (mg/cm³)	L3 (mg/cm³)	L1 (mg/cm³)	L2 (mg/cm³)	L3 (mg/cm³)
12	120 kVp	54.5 ± 0.4	107.3 ± 0.4	205.7 ± 0.5	54.6 ± 0.4	107.4 ± 0.4	206.2 ± 0.3
	76 keV	47.5 ± 1.0	98.6 ± 0.5	192.3 ± 0.4	47.6 ± 0.7	99.1 ± 0.6	192.5 ± 0.5
	75 keV	48.5 ± 1.1	100.6 ± 0.7	195.4 ± 1.8	48.4 ± 0.7	100.9 ± 0.5	196.4 ± 0.5
	74 keV	49.4 ± 1.0	102.7 ± 0.5	200.0 ± 0.8	49.5 ± 0.7	103.1 ± 0.2	200.3 ± 0.4
	73 keV	50.7 ± 1.0	104.9 ± 0.7	204.1 ± 0.6	51.0 ± 1.0	105.4 ± 0.6	204.8 ± 0.7
	72 keV	52.0 ± 1.2	107.1 ± 0.8	208.9 ± 0.7	51.9 ± 0.9	107.7 ± 0.7	208.8 ± 0.5
15	120 kVp	54.6 ± 0.4	107.2 ± 0.6	205.8 ± 0.5	54.5 ± 0.2	107.6 ± 0.3	206.2 ± 0.8
	76 keV	47.1 ± 1.2	98.6 ± 0.8	191.5 ± 0.6	47.3 ± 1.0	98.9 ± 0.6	191.9 ± 0.5
	75 keV	48.0 ± 0.7	100.5 ± 0.3	195.2 ± 0.7	48.2 ± 1.0	100.6 ± 0.3	195.2 ± 0.8
	74 keV	49.2 ± 1.1	102.6 ± 0.3	198.9 ± 0.7	49.1 ± 0.8	102.4 ± 0.3	199.3 ± 0.6
	73 keV	50.3 ± 0.8	105.0 ± 0.8	203.0 ± 0.5	50.0 ± 0.6	104.7 ± 0.3	203.8 ± 0.4
	72 keV	51.3 ± 0.8	106.9 ± 0.8	207.5 ± 0.5	51.4 ± 0.8	107.7 ± 0.5	208.1 ± 0.6
24.4	120 kVp	54.7 ± 0.4	108.1 ± 0.2	206.8 ± 0.6	55.0 ± 0.4	108.2 ± 0.2	207.1 ± 0.4
	76 keV	47.4 ± 0.2	98.0 ± 0.2	191.9 ± 0.1	47.3 ± 0.2	98.1 ± 0.2	192.2 ± 0.2
	75 keV	48.4 ± 0.2	99.8 ± 0.4	195.3 ± 0.2	48.3 ± 0.1	100.0 ± 0.1	195.8 ± 0.1
	74 keV	49.3 ± 0.1	101.8 ± 0.3	199.1 ± 0.3	49.3 ± 0.2	101.6 ± 0.1	199.5 ± 0.1
	73 keV	50.4 ± 0.3	103.6 ± 0.2	203.0 ± 0.2	50.4 ± 0.3	103.9 ± 0.2	203.5 ± 0.2
	72 keV	51.4 ± 0.2	105.8 ± 0.1	207.5 ± 0.3	51.5 ± 0.2	106.1 ± 0.4	207.9 ± 0.4

Table 4. BMD measurements based on 120-kVp images and VMIs at 72–76 keV. The data is presented as mean ± standard deviation. *BMD* bone mineral density, *ROI* region of interest, *VMI* virtual monochromatic image, *kVp* peak tube voltage.

results showed that BMD measurements based on 120-kVp images were higher than the true HA concentration of the corresponding vertebral inserts (P < 0.001).

There was no statistical difference between BMD values measured based on part of VMIs and the true HA concentration (Table S1): (1) For default ROI and 12 mGy, BMD measurements based on VMIs at 73–74 keV showed no statistical difference with HA concentration in the L1 ($P_{74keV} = 0.244$, $P_{73keV} = 0.684$); (2) For default ROI and 12 mGy, there was no statistical difference between BMD measurements based on 75-keV VMI and HA concentration in L2 (P = 0.139); (3) For default ROI and 12 mGy, there was no statistical difference between BMD measurements based on 74-keV VMI and HA concentration in L3 (P = 0.976); (4) For default ROI and 15 mGy, there was no statistical difference between BMD measurements based on VMIs at 73–74 keV and HA concentration in L1 ($P_{74keV} = 0.193$, $P_{73keV} = 0.467$); (5) For default ROI and 24.4 mGy, there was no statistical difference between BMD measurements based on 73-keV VMI and HA concentration in L1 (P = 0.08); (6) For default ROI and 24.4 mGy, there was no statistical difference between BMD measurements based on 75-keV

5
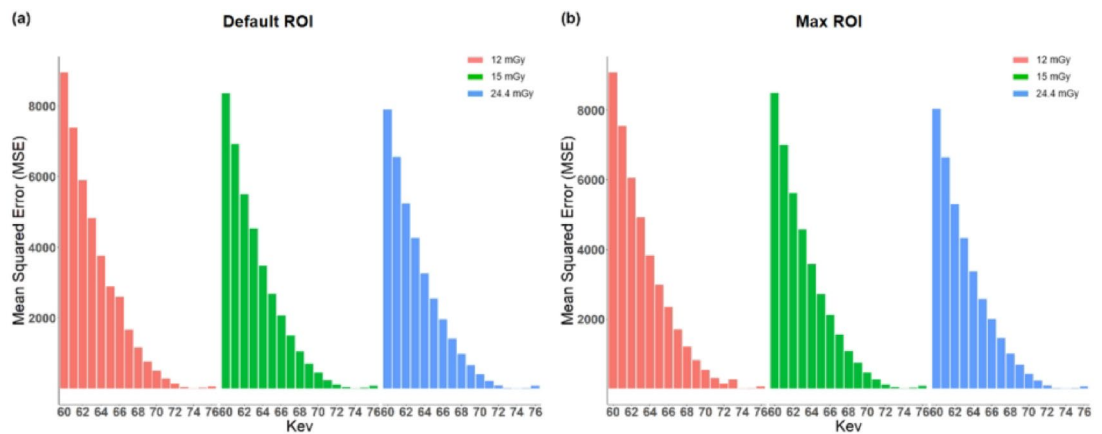
Fig. 3. The *MSE* of BMD measurements based on VMIs at 60–76 keV. *BMD* bone mineral density, *MSE* mean squared error, *ROI* region of interest, *VMI* virtual monochromatic image.

VMI and HA concentration in L2 ($P = 0.289$); (7) For max ROI and 12 mGy, there was no statistical difference between BMD measurements based on VMIs at 73–74 keV and HA concentration in L1 ($P_{74keV} = 0.210$, $P_{73keV} = 0.092$); (8) For max ROI and 12 mGy, there was no statistical difference between BMD measurements based on 74-keV VMI and HA concentration in L3 ($P = 0.235$); (9) For max ROI and 15 mGy, there was no statistical difference between BMD measurements based on VMIs at 73–74 keV and HA concentration in L1 ($P_{74keV} = 0.071$, $P_{73keV} = 0.910$); (10) For max ROI and 15 mGy, there was no statistical difference between BMD measurements based on 74-keV VMI and HA concentration in L3 ($P = 0.054$); (11) For max ROI and 24.4 mGy, there was no statistical difference between BMD measurements based on 75-keV VMI and HA concentration in L2 ($P = 0.846$).

To maintain control over variables and ensure measurement stability, OLS regression was used to explore the optimal VMI level. The results of OLS regression showed that 74-keV VMI had the lowest *MSE* with different ROI sizes and radiation doses (Fig. 3). The lowest *MSE* indicates that the disparity between bone mineral density (BMD) values obtained from the 74-keV VMI and the actual hydroxyapatite (HA) concentration is minimal, thereby signifying optimal measurement stability.

Discussion

In this phantom study, we found that BMD measurements based on clinically commonly used 120-kVp images were slightly higher than HA concentrations in vertebrae. In addition, 74-keV VMI provided the most accurate and stable measurement of BMD, which provide immediately applicable guidance for centers utilizing existing QCT workflows.

Despite emerging alternatives, QCT is widely used in diagnosing and studying osteoporosis because it can measure the true volumetric BMD without being affected by other overlapping organs[4]. There are three commonly used QCT systems for BMD measurement[13]: (1) Synchronous calibration phantom-based system; (2) Asynchronous calibration phantom-based system; (3) Self-calibration phantom-less system. Synchronous calibration phantom-based systems require a phantom to be placed under the subject's body during scanning to correct the formula for attenuation values and BMD measurements, but are generally more susceptible to beam hardening and scattering effects[14]. The asynchronous calibration phantom-based system, used in our study, performs phantom-based calibration before scanning, thus avoiding errors caused by phantoms during scanning[15]. Self-calibration phantom-less systems are a recent research trend, using the subject's own fat and muscle attenuation as the reference to calculate BMD values[16,17]. However, regardless of the QCT system used, achieving a 100% match between BMD measurements and true HA concentration is still challenging due to the inherent limitations of CT imaging principles.

In routine clinical QCT, BMD is measured with polychromatic X-rays (120-kVp)[18]. Due to the beam hardening effect, lower energy photons are preferentially absorbed by tissues as X-rays traverse the human body, leads to an elevation in the average energy of the rays and instability in CT values. Similarly, in our study, although the QCT system software was calibrated with the standard calibration phantom (model 4) at the beginning of this study, there was still a deviation in the BMD measurement of ESP based on 120-kVp images. This inconsistency could stem from differences in the volumes of the two models and the varying impact of beam hardening effects caused by peripheral substances[5,19]. Consequently, our study revealed that 120-kVp images overestimated BMD values, which may also occur in routine clinical examinations.

VMIs reconstructed by DECT based on high and low energy datasets can effectively reduce the beam-hardening artifacts and anti-correlated noise, and VMIs at 65–75 keV have similar image quality and attenuation compared with 120-kVp images, suggesting that VMI has application value in BMD measurement based on QCT[20–23]. In light of these observations, we opted to explore a broader energy range (60–76 keV) as far as possible for exploration under the premise that the work load was feasible. Our results showed that VMIs at specific energy levels are able to obtain more accurate BMD measurements than 120-kVp images at different ROI sizes and radiation doses. In particular, we identified the 74-keV VMI as offering optimal measurement stability

while maintaining acceptable accuracy. This finding may provide reference for subsequent relevant research and clinical applications.

In addition, our study identified ROI size and radiation dose as influential factors affecting BMD measurements, which is consistent with the results of previous studies[5]. Due to the change of radiation dose, the attenuation value of bone trabecula will change, and the BMD value based on the attenuation value will change[24]. Changes in ROI affect the number of voxels included in the calculation, and the attenuation value of some voxels is affected by a partial volume effect, which can also lead to a bias in BMD values[25]. These observations underscore the importance for clinicians to minimize measurement errors attributed to these factors when utilizing QCT for BMD assessment, aiming for greater stability and accuracy.

Beyond virtual monochromatic imaging, emerging technologies such as photon-counting detector CT (PCD-CT) and artificial intelligence (AI) promise to further enhance QCT-based BMD measurement accuracy. PCD-CT, with its superior energy resolution and material decomposition capabilities, minimizes beam-hardening artifacts and enables precise calcium quantification ($r = 0.99$ in hydroxyapatite phantoms), as demonstrated in osteoporosis models[26,27]. These advancements align with our findings on VMI energy optimization (e.g., 74 keV), suggesting synergistic potential for integrating spectral imaging techniques. Meanwhile, AI-driven approaches, including deep-learning image reconstruction, improve spatial resolution and reduce noise without compromising BMD accuracy[28]. While our study focused on optimizing VMI energy levels for conventional DECT, future work could combine PCD-CT's spectral sensitivity with AI-enhanced protocols to address limitations in clinical standardization. Such integration may establish next-generation QCT systems capable of simultaneous structural and quantitative bone assessment, bridging the gap between phantom-based research and patient-specific applications.

There are some limitations to this study. First, our findings are based on a specific CT system. Different manufacturers and types of DECT systems have been shown to have different BMD measurement accuracy[29,30]. Furthermore, while emerging PCD-CT technology has shown promise in osteoporosis screening through simultaneous 3D structural imaging and calcium-water component analysis[27], its performance relative to DECT-derived VMIs remains unvalidated in human subjects. Future studies should integrate PCD-CT's material decomposition capabilities with VMI energy optimization strategies to develop more robust QCT workflows. Therefore, the optimal VMI energy level for other DECT systems requires further validation. Second, our study only considers VMIs at 60–76 keV, as it has previously been reported that VMIs obtained in this range are comparable to conventional 120-kVp images. In fact, the maximum range of VMI levels that can be reconstructed by DECT is 40–200 keV[31]. Although BMD measurements decrease with increasing energy levels according to our study, it is not known whether this change applies to VMI level beyond 60–76 keV. Finally, when applying the findings of this study clinically, it is important to note that BMD measurements in clinical subjects tend to be influenced by more factors (position, adipose tissue, etc.), which may alter the optimal VMI level[32,33].

In conclusion, when measuring BMD values based on QCT, VMI can reduce the measurement error and improve the accuracy compared with the conventional 120-kVp images. In particular, the 74-keV VMI demonstrated superior measurement stability and reliable accuracy in this study. Our findings provide immediately applicable guidance for centers utilizing existing QCT workflows while establishing foundational knowledge for future spectral CT applications.

Data availability

The datasets generated during and/or analyzed during the current study are available from the corresponding author (J.T., Z.L.) on reasonable request.

References
1. Lin, W. et al. Quantitative CT screening improved lumbar BMD evaluation in older patients compared to dual-energy X-ray absorptiometry. *BMC Geriatr.* **23**, 231 (2023).
2. Mao, S. S. et al. Thoracic quantitative computed tomography (QCT) can sensitively monitor bone mineral metabolism: Comparison of thoracic QCT vs lumbar QCT and dual-energy X-ray absorptiometry in detection of age-relative change in bone mineral density. *Acad. Radiol.* **24**, 1582–1587 (2017).
3. Barmpa, E. et al. Bone mineral density in adult patients with type 1 diabetes mellitus assessed by both DXA and QCT. *J. Diabetes Res.* **2023**, 8925956 (2023).
4. Yu, J. S. et al. ACR appropriateness criteria(R) osteoporosis and bone mineral density: 2022 Update. *J. Am. Coll. Radiol.* **19**, S417–S432 (2022).
5. Brunnquell, C. L., Winsor, C., Aaltonen, H. L. & Telfer, S. Sources of error in bone mineral density estimates from quantitative CT. *Eur. J. Radiol.* **144**, 110001 (2021).
6. Abu-Omar, A. et al. Utility of dual-energy computed tomography in clinical conundra. *Diagnostics.* **14**, 775 (2024).
7. Matsumoto, K. et al. Virtual monochromatic spectral imaging with fast kilovoltage switching: improved image quality as compared with that obtained with conventional 120-kVp CT. *Radiology* **259**, 257–262 (2011).
8. van Hamersvelt, R. W. et al. Accuracy of bone mineral density quantification using dual-layer spectral detector CT: A phantom study. *Eur. Radiol.* **27**, 4351–4359 (2017).
9. Mei, K. et al. Bone mineral density measurements in vertebral specimens and phantoms using dual-layer spectral computed tomography. *Sci. Rep.* **7**, 17519 (2017).
10. GmbH, Q. *European Spine Phantom (ESP).* [cited] Available from: https://www.qrm.de/en/products/european-spine-phantom (2024).
11. Kalender, W. A. et al. The European Spine Phantom—A tool for standardization and quality control in spinal bone mineral measurements by DXA and QCT. *Eur. J. Radiol.* **20**, 83–92 (1995).
12. China, N. H. C. *Requirements for Radiological Protection in Diagnostic Radiology.* [cited] Available from: http://www.nhc.gov.cn/wjw/pcrb/202004/3db780ee6ba84d699d198da17f6f74d4/files/67d5d27c85814d118009e5671b795f63.pdf (2020).

13. Engelke, K., Chaudry, O. & Bartenschlager, S. Opportunistic screening techniques for analysis of CT scans. *Curr. Osteoporos. Rep.* **21**, 65–76 (2023).
14. Loffler, M. T. et al. X-ray-based quantitative osteoporosis imaging at the spine. *Osteoporos. Int.* **31**, 233–250 (2020).
15. Qadan, L. & Ahmed, A. Addressing gaps in osteoporosis screening in Kuwait using opportunistic quantitative computer tomography (QCT): A retrospective study. *Arch. Osteoporos.* **18**, 50 (2023).
16. Liu, Z. J. et al. Automatic phantom-less QCT system with high precision of BMD measurement for osteoporosis screening: Technique optimisation and clinical validation. *J. Orthop. Transl.* **33**, 24–30 (2022).
17. Prado, M., Khosla, S., Chaput, C. & Giambini, H. Opportunistic application of phantom-less calibration methods for fracture risk prediction using QCT/FEA. *Eur. Radiol.* **31**, 9428–9435 (2021).
18. Engelke, K. et al. Clinical use of quantitative computed tomography and peripheral quantitative computed tomography in the management of osteoporosis in adults: The 2007 ISCD Official Positions. *J. Clin. Densitom.* **11**, 123–162 (2008).
19. Carpenter, R. D. et al. Inter-scanner differences in in vivo QCT measurements of the density and strength of the proximal femur remain after correction with anthropomorphic standardization phantoms. *Med. Eng. Phys.* **36**, 1225–1232 (2014).
20. Sato, K. et al. Accuracy of virtual monochromatic images generated by the decomposition of photoelectric absorption and Compton scatter in dual-energy computed tomography. *Phys. Eng. Sci. Med.* **45**, 239–249 (2022).
21. Tanoue, S. et al. Virtual monochromatic image quality from dual-layer dual-energy computed tomography for detecting brain tumors. *Korean J. Radiol.* **22**, 951–958 (2021).
22. van Ommen, F. et al. Image quality of virtual monochromatic reconstructions of noncontrast CT on a dual-source CT scanner in adult patients. *Acad. Radiol.* **28**, e323–e330 (2021).
23. Lenga, L. et al. Can dual-energy CT-based virtual monoenergetic imaging improve the assessment of hypodense liver metastases in patients with hepatic steatosis?. *Acad. Radiol.* **28**, 769–777 (2021).
24. Garner, H. W., Paturzo, M. M., Gaudier, G., Pickhardt, P. J. & Wessell, D. E. Variation in attenuation in L1 trabecular bone at different tube voltages: Caution is warranted when screening for osteoporosis with the use of opportunistic CT. *AJR Am. J. Roentgenol.* **208**, 165–170 (2017).
25. Lee, D. C., Hoffmann, P. F., Kopperdahl, D. L. & Keaveny, T. M. Phantomless calibration of CT scans for measurement of BMD and bone strength-inter-operator reanalysis precision. *Bone* **103**, 325–333 (2017).
26. Willemink, M. J., Persson, M., Pourmorteza, A., Pelc, N. J. & Fleischmann, D. Photon-counting CT: Technical principles and clinical prospects. *Radiology* **289**, 293–312 (2018).
27. Bhattarai, A., Tanaka, R., Yeung, A. W. K. & Vardhanabhuti, V. Photon-counting CT material decomposition in bone imaging. *J. Imaging.* **9**, 209 (2023).
28. Li, Y. et al. Deep-learning image reconstruction for image quality evaluation and accurate bone mineral density measurement on quantitative CT: A phantom-patient study. *Front. Endocrinol.* **13**, 884306 (2022).
29. Zhao, Y. et al. Accuracy, linearity and precision of spine QCT vBMD phantom measurements for different brands of CT scanner: A multicentre study. *J. Clin. Densitom.* **25**, 34–42 (2022).
30. Engelke, K. Quantitative computed tomography-current status and new developments. *J. Clin. Densitom.* **20**, 309–321 (2017).
31. Jia, Z. et al. Performance of dual-layer spectrum CT virtual monoenergetic images to assess early rectal adenocarcinoma T-stage: Comparison with MR. *Insights Imaging.* **15**, 11 (2024).
32. Cheng, X. et al. The accurate relationship between spine bone density and bone marrow in humans. *Bone* **134**, 115312 (2020).
33. Szczykutowicz, T. P., DuPlissis, A. & Pickhardt, P. J. Variation in CT number and image noise uniformity according to patient positioning in MDCT. *AJR Am. J. Roentgenol.* **208**, 1064–1072 (2017).

Author contributions

Y.Z. and Y.S. were mainly responsible for data acquisition, analysis and manuscript writing. Z.L. and J.T. were mainly responsible for the idea, supervision, and fund application. Z.C. and P.Y. were responsible for calibration before the study. Z.Y. was responsible for the revising the manuscript. T.L. was responsible for the statistical analysis. All authors reviewed the final manuscript.

Funding

Declarations

Competing interests

The authors declare no competing interests.

Additional information

Supplementary Information The online version contains supplementary material available at https://doi.org/10.1038/s41598-025-06014-9.

Correspondence and requests for materials should be addressed to Z.L. or J.T.

Reprints and permissions information is available at www.nature.com/reprints.

Publisher's note Springer Nature remains neutral with regard to jurisdictional claims in published maps and institutional affiliations.